Mon. Not. R. Astron. Soc. **365,** 1263–1276 (2006) doi:10.1111/j.1365-2966.2005.09806.x

Structural properties of the M31 dwarf spheroidal galaxies

A. W. McConnachie[1,2]★ and M. J. Irwin[1]

[1]*Institute of Astronomy, Madingley Road, Cambridge, CB3 0HA*
[2]*Department of Physics and Astronomy, University of Victoria, Victoria, BC V8P 5C2, Canada*

Accepted 2005 October 31. Received 2005 October 28; in original form 2005 August 30

ABSTRACT

The projected structures and integrated properties of the Andromeda I, II, III, V, VI, VII and Cetus dwarf spheroidal galaxies are analysed based upon resolved counts of red giant branch stars. The observations were taken as part of the Isaac Newton Telescope Wide Field Survey of M31 and its environs. For each object, we have derived isopleth maps, surface brightness profiles, intensity-weighted centres, position angles, ellipticities, tidal radii, core radii, concentration parameters, exponential scalelengths, Plummer scalelengths, half-light radii, absolute magnitudes and central surface brightnesses. Our analysis probes into larger radius and fainter surface brightnesses than most previous studies, and as a result we find that the galaxies are generally larger and brighter than has previously been recognized. In particular, the luminosity of Andromeda V is found to be consistent with the higher metallicity value which has been derived for it. We find that exponential and Plummer profiles provide adequate fits to the surface brightness profiles, although the more general King models provide the best formal fits. Andromeda I shows strong evidence of tidal disruption and S-shaped tidal tails are clearly visible. On the other hand, Cetus does not show any evidence of tidal truncation, let alone disruption, which is perhaps unsurprising given its isolated location. Andromeda II shows compelling evidence of a large excess of stars at small radius and suggests that this galaxy consists of a secondary core component, in analogy with recent results for Sculptor and Sextans. Comparing the M31 dwarf spheroidal population with the Galactic population, we find that the scaleradii of the M31 population are larger than those for the Galactic population by at least a factor of 2, for all absolute magnitudes. This difference is either due to environmental factors or due to orbital properties, suggesting that the ensemble average tidal field experienced by the M31 dwarf spheroidals is weaker than that experienced by the Galactic dwarf spheroidals. We find that the two populations are offset from one another in the central surface brightness – luminosity relation, which is probably related to this difference in their scale sizes. Finally, we find that the M31 dwarf spheroidals show the same correlation with distance from host as shown by the Galactic population, such that dwarf spheroidals with a higher central surface brightness are found further from their host. This again suggests that environment plays a significant role in dwarf galaxy evolution, and requires detailed modelling to explain the origin of this result.

Key words: galaxies: dwarf – galaxies: fundamental parameters – galaxies: general – galaxies: interactions – Local Group – galaxies: structure.

1 INTRODUCTION

Most of our detailed knowledge on the structure of dwarf spheroidal (dSph) galaxies comes from observations of the nine[1] dSphs which make up part of the Galactic satellite system. Irwin & Hatzidimitriou (1995) (hereafter IH95) analysed the structure of the Galactic dSphs, except Sagittarius, by mapping their resolved star counts from photographic plates. They found that the stellar profiles of the dSphs were generally well described by a single component King or exponential model. A generic feature was an excess of stars at large radii, over and above that expected from the best-fitting King tidal model, which have generally been interpreted as evidence for tidal disturbance. A King profile is not a physically motivated model for dSphs since their relaxation time is of the order of Hubble time, and their stellar velocity distribution may deviate significantly from the Maxwellian. Any interpretation of the structure of a dSph based

★E-mail: alan@uvic.ca

[1] Willman et al. (2005) have recently discovered a new Galactic companion in Ursa Major, which is not included here.

exclusively on a King model fit must therefore be treated with caution. Nevertheless, such analyses do yield a useful parametrization, and in particular the equivalent half-light radius can readily be compared with alternative parametrizations derived from Plummer or exponential profiles. The King model tidal radii (r_t) of the Galactic dSphs are of the order of 1 kpc, and their average half-light radius ($r_{\frac{1}{2}}$) is $\sim$170 pc, although Fornax is over twice this size. More recent work on the radial profiles of Galactic dSphs from wide field CCD cameras (Ursa Minor: Majewski et al. 2000; Martínez-Delgado et al. 2001; Draco: Odenkirchen et al. 2001; Carina: Palma et al. 2003) generally confirms the results from earlier photographic studies.

Some recent studies have revealed that the structures of dSphs are more complex than had previously been assumed. Harbeck et al. (2001) looked for spatial variations in the colour of the red giant branch (RGB) and the horizontal branch of several Local Group dSphs and found evidence for horizontal branch population gradients in many of their systems. Tolstoy et al. (2004) have shown that Sculptor has a spatially, chemically and kinematically distinct second component, in the form of a centrally concentrated core. Additionally, Kleyna et al. (2004) have shown that the Sextans dSph has a kinematically cold core, and that Ursa Minor has a distinct concentration of stars offset from its geometric centre which has distinct kinematics (IH95; Kleyna et al. 2003).

Given these recent findings in the Galactic dSph system, it is timely to look at the next closest dSph system to our own, that of M31. Approximately 16 satellites make up this subsystem, of which seven – Andromeda I, II, III, V, VI, VII and IX – are classified as dSphs. Andromeda I, II and III were discovered by Sidney van den Bergh in his pioneering survey for Local Group galaxies in the early 1970s (van den Bergh 1972a,b; 1974), together with Andromeda IV, an object which was later shown to be a background galaxy (Ferguson, Gallagher & Wyse 2000). Andromeda V and VI were discovered some years later by Armandroff, Davies & Jacoby (1998) and Armandroff, Jacoby & Davies (1999) from a detailed analysis of the digitized Second Palomar Sky Survey. At the same time, Andromeda VI was discovered independently by Karachentsev & Karachentseva (1999) along with Andromeda VII. An additional object, Andromeda VIII (Morrison et al. 2003), has recently been postulated to be associated with an over density of planetary nebulae in the giant stellar stream visible in the south-east of M31 (Ibata et al. 2001), although the nature of this over density remains unclear. Andromeda IX was recently discovered by Zucker et al. (2004) and is the faintest satellite of M31 yet known, with $M_v \simeq -8.3$.

In comparison to the dSphs which orbit the Galaxy, relatively little is known in detail about the stellar populations of the Andromeda dSphs. From the colour of their RGBs, it would appear that all of them are metal poor [Fe/H] $\lesssim -1.5$ dex (e.g. McConnachie et al. 2005). Deep *Hubble Space Telescope* (*HST*) fields for Andromeda I, II and III reaching below the horizontal branch (Da Costa et al. 1996, 2000; Da Costa, Armandroff & Caldwell 2002) show extended epochs of star formation and variations in horizontal branch morphology, suggesting the star formation histories have been notably different. In addition, Andromeda I is observed to display a gradient in its horizontal branch morphology, such that there are more blue horizontal branch stars located at larger radius from the centre of the dwarf (Da Costa et al. 1996). Some evidence for asymptotic giant branch (AGB) components have also been seen in these systems (most recently by Harbeck, Gallagher & Grebel 2004 and Kerschbaum et al. 2004), although a strong intermediate age component similar to some of the Galactic dSphs is generally lacking.

As a compliment to the deeper pointed *HST* observations, we have obtained wide field Johnston V (V') and Gunn i (i') photometry for the majority of the members of the M31 subgroup using the Wide Field Camera (WFC) on the 2.5-m Isaac Newton Telescope (INT). This is a four-chip EEV 4K $\times$ 2K CCD mosaic camera with a $\sim$0.29 square degree field of view (Walton et al. 2001). With typical exposures of $\sim$1000 s in each passband, this photometry is deep enough to observe the top few magnitudes of the RGB in each system and has already been used to derive a homogeneous set of distance and metallicity estimates for each of these galaxies (McConnachie et al. 2004, 2005). Here, we use the same data to analyse the structural properties of each of the Andromeda dSphs as well as the isolated dSph in Cetus as a comparison. In common with Tucana, this galaxy is one of only two dSphs not found as a satellite to a large galaxy in the Local Group. Our results for Andromeda IX are presented elsewhere (Chapman et al. 2005). Our overall technique and methodology are similar to that adopted by IH95 for the Galactic dSphs, insofar as we base most of our analysis on resolved star counts. Caldwell et al. (1992) and Caldwell (1999) have performed a similar analysis for the Andromeda dSphs based upon the integrated light, and we will compare our results to these later (Section 4.1).

In Section 2, we derive contour maps, radial profiles and associated structural parameters for Andromeda I, II, III, V, VI, VII and Cetus based upon resolved star counts. The integrated luminosities, central surface brightnesses and related quantities are derived in Section 3. We postpone discussion of all the results until Section 4, which also compares the M31 dSph population to the Galactic dSph population. Section 5 summarizes and concludes.

2 STAR COUNTS AND STRUCTURE

2.1 Preliminaries

The reader is referred to Ferguson et al. (2002) and McConnachie et al. (2004, 2005) for information on our observing strategy and data reduction process. We do, however, recap here the morphological photometric classification procedure for each detected source, as this is central to our subsequent analysis.

Object classification. Objects are classified independently in each passband based on their overall morphological properties, specifically their ellipticity as derived from intensity-weighted second moments and the curve of growth of their flux distribution (Irwin et al. 2004). Measures from these are combined to produce a normalized $N(0,1)$ statistic which compares the likeness of each object to the well-defined stellar locus visible on each frame. Stellar objects are generally chosen to lie within 2 or 3σ of this locus depending on the desired trade-off between completeness and contamination from non-stellar objects. Contamination takes the form of a small number of spurious images which are essentially eliminated by requiring objects to be detected on both passbands. Additionally, at faint magnitudes (within $\simeq$1–2 mag of the frame limit depending on seeing), distant compact galaxies may also be incorrectly identified as stellar images. This is particularly true in bluer passbands. For this specific study, completeness is more important than mild non-stellar contamination. We therefore use all objects identified in the INT WFC that lie within 3σ of the stellar locus in the i' band, and require only that the object has been detected in the V' band within 1 arcsec of the i'-band position, to reduce contamination from background galaxies.

Background corrections. A good estimate of the background contamination and its uncertainty is vital to accurately determining the extent and profile of each dSph. The term 'background' describes both Galactic foreground stars and distant compact galaxies. These

are minimized in the first instance by using simple cuts in colour – magnitude space, designed to isolate the RGB and remove those stars whose colour and magnitude make membership of the dSph unlikely. This is illustrated for Andromeda II in Fig. 1. A horizontal cut in i' magnitude, coincident with the derived location of the tip of the RGB (TRGB), removes objects too bright to be RGB stars in the dSph. Two cuts on the blue and red side of the RGB also remove objects whose colour makes membership of the dSph unlikely. This process removes a significant fraction of the Galactic foreground.

Although the influence of compact galaxies is significantly reduced by the morphological classification/selection scheme, it cannot be completely removed at faint magnitudes. A statistical correction must therefore be applied to remove the remaining contamination. This is estimated by excising the dSph from a pixelated map of the stellar spatial distribution. An intensity distribution is constructed from the remaining pixels, and a sigma-clipped least-squares fit of a Gaussian profile is performed on this 'background' distribution to calculate the position of the peak (i.e. the background level) and associated errors in the usual way. As we do not know the full extent of the dSph a priori, the correct subtraction of the dwarf component requires several attempts before we are left with the easily identifiable background component to perform the fit to. We do not require to simultaneously fit the dwarf profile plus background because the background is relatively flat over the area of the field, with no evidence of strong differential extinction for any of the dwarfs which would affect this measurement. For large dSphs which cover the majority of the field of view (Andromeda II, VII and Cetus), the background estimate will suffer from contamination from the outer regions of these objects. This effect is generally small, as the number density of stars belonging to the dSph at large radius is much smaller than the background contamination. However, this effect will lead to a slight overestimate of the background by a few per cent, resulting in a marginal steepening of the outer parts of the derived profile. The level of this effect is small enough to be covered by the derived uncertainties on the scaleradii, and will always act to underestimate the actual values of these parameters.

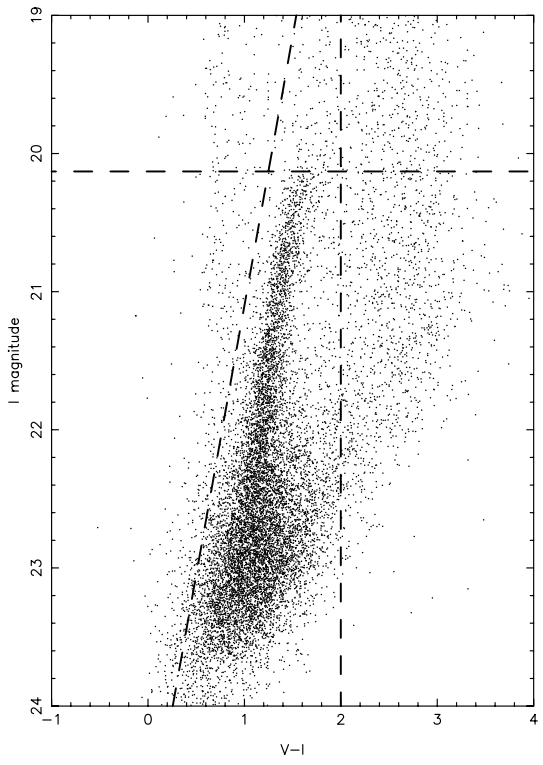

Figure 1. A colour magnitude diagram of Andromeda II in Landolt V and I. The dashed lines represent the cuts that we use in order to reduce background contamination. The horizontal cut is at the location of the TRGB derived in McConnachie et al. (2004) and McConnachie & Irwin (2006). The other two cuts are placed so as to isolate the RGB loci as shown.

Crowding corrections. In the central regions of the dSphs, the higher density of images causes some individual sources to remain unresolved. This can be approximately corrected for by using the crowding correction of Irwin & Trimble (1984):

$$f' \simeq f\left(1 + 2fA' + \frac{16}{3}f^2A'^2 + \cdots\right), \quad (1)$$

where f is the observed number density of all images (not just stellar), f' is the actual number density and A' is the typical area of the image, where the radius of the image is closely approximated by the seeing. For the INT WFC observations, the typical seeing is $\simeq$1 arcsec. The derivation and validity of equation (1) is given in the appendix of Irwin & Trimble (1984) and ignores second-order effects such as the actual shape of the luminosity function. For the dSphs, the typical background stellar densities are $\sim$2–3 stars arcmin^{-2} (after photometric cuts have been applied) and are unchanged by the crowding correction. The crowding correction increases the stellar counts in the central regions of the dSphs by typically 5–10 per cent.

2.2 Isopleths and dwarf geometry

A field of $0\overset{\circ}{.}5 \times 0\overset{\circ}{.}5$ containing the dSph is used for each isopleth map. For Andromeda II, V, VI, VII and Cetus, this corresponds closely to the INT WFC pointing, and the north-west corner is missing in each case due to the geometry of the CCDs. For Andromeda I and III, multiple pointings of the camera are combined to form a mosaic. For each object, the field is divided into $\sim$100 $\times$ 100 pixel ($\simeq$18-arcsec resolution), and the crowding correction is applied based upon the source density in each cell. The isopleth maps of the stellar sources are constructed, smoothed and displayed in Fig. 2. For the two fields constructed from multiple INT WFC pointings, faint-end threshold magnitudes have been used to account for varying incompleteness levels between fields due to different observing conditions. Contour levels in Fig. 2 are set such that each subsequent increment is a factor of n greater than the previous increment, where the first increment is 2σ above the background. n is different for each system and is given in the caption of Fig. 2. This allows the same number of contours to be used for each dwarf galaxy, making visual comparison of their morphologies easier. The 2σ contour also picks out the peaks of noise features as well as the dSph, and gives a general indication of the quality of the background subtraction.

For each isophote, we calculate the centre of gravity, (x_o, y_o), position angle, θ (measured east from north), and eccentricity, e, by using the intensity-weighted moments. Thus,

$$x_o = \frac{\sum_i x_i I(x_i,\, y_i)}{\sum_i I(x_i,\, y_i)}, \quad y_o = \frac{\sum_i y_i I(x_i,\, y_i)}{\sum_i I(x_i,\, y_i)},$$

$$\theta = \frac{1}{2}\arctan\frac{2\sigma_{xy}}{\sigma_{yy} - \sigma_{xx}},$$

$$e = \frac{\sqrt{(\sigma_{xx} - \sigma_{yy})^2 + 4\sigma_{xy}^2}}{\sigma_{xx} + \sigma_{yy}}, \quad (2)$$

where $I(x_i, y_i)$ is the intensity of the ith pixel and σ_{xx}, σ_{yy} and σ_{xy} are the intensity-weighted second moments within each isophotes.

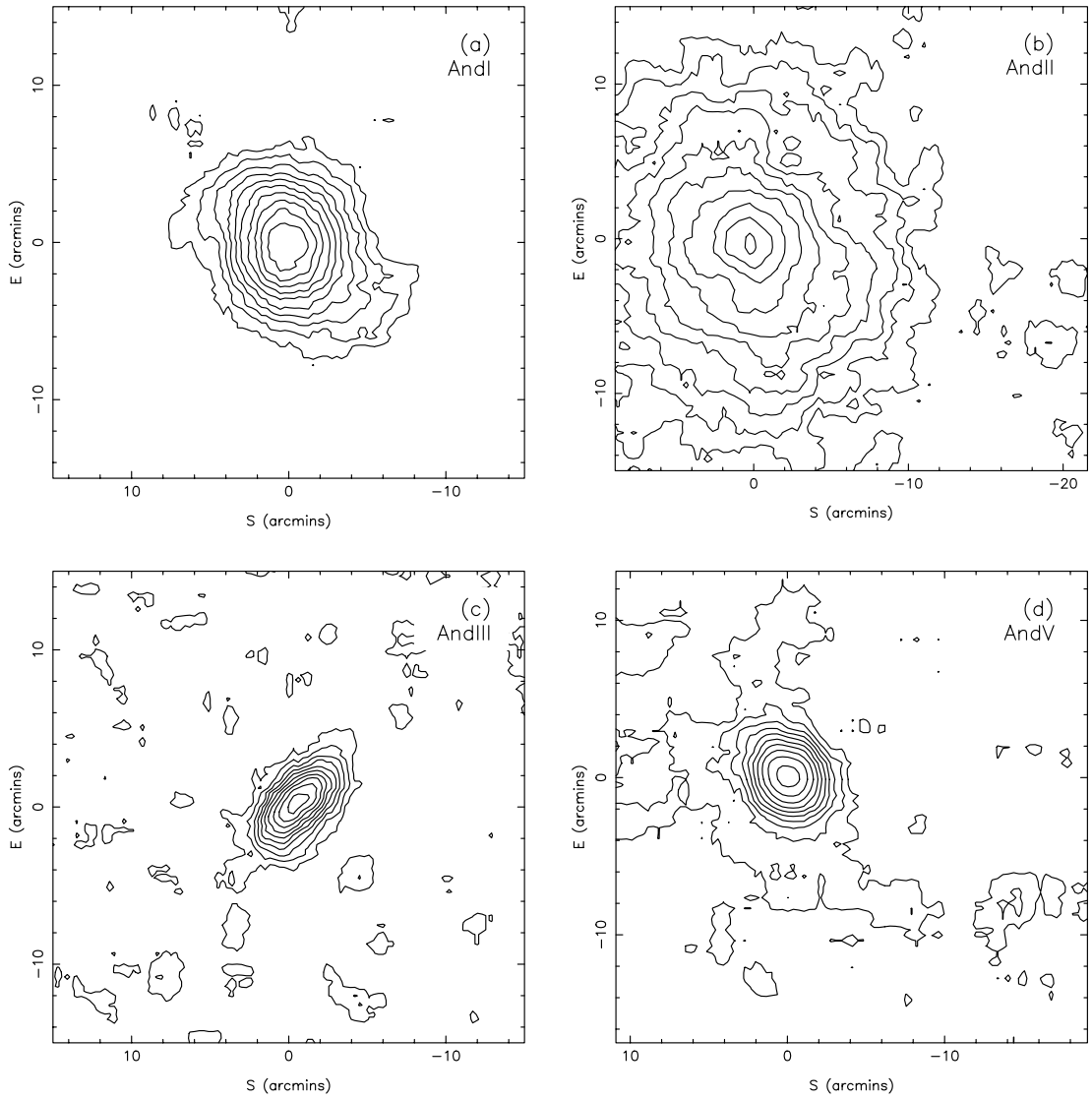

Figure 2. Isopleth maps for the six dSph satellites of M31 (panels a–f), and the isolated dSph in Cetus (g), in standard coordinate (ξ, η) projections. Each map shows a similar $0\overset{\circ}{.}5 \times 0\overset{\circ}{.}5$ area of sky. A large range in structural properties is clearly evident for these galaxies. The first contour of each map is 2σ above background. Contour increments then increase by a factor of n for each subsequent contour. (a) Andromeda I: $n = 1.15$ (b) Andromeda II: $n = 1.3$ (c) Andromeda III: $n = 1.15$ (d) Andromeda V: $n = 1.15$ (e) Andromeda VI $n = 1.25$ (f) Andromeda VII: $n = 1.33$ (g) Cetus: $n = 1.25$.

The eccentricity is related to the ellipticity, $\epsilon = 1 - b/a$, via

$$\epsilon = 1 - \sqrt{\frac{1-e}{1+e}}. \tag{3}$$

The 'average' parameters for each dSph are then estimated from the values derived for each isophote, and the uncertainty estimated from the variation in the parameters as a function of isophotal threshold. This procedure gives estimates of θ and ϵ that are independent of any parametrization, and allows a more robust estimate of their uncertainties. Effects such as isophote rotation are likewise able to be quantified for those systems where such an effect is taking place. The results of this analysis are tabulated in Table 1.

2.3 Radial profiles and associated parameters

The stellar radial profile for each galaxy is constructed by measuring the stellar number density in elliptical annuli with the average ellipticity and position angle derived above and applying the background correction. Assuming fixed parameters for each galaxy gives a robust estimate of the profile suitable for comparison with other galaxies and models. The width of the elliptical annuli is set by requiring a minimum signal-to-noise ratio threshold in each bin. The results are plotted in logarithmic form in Fig. 3. The error bars take into account the Poisson error in the counts and the uncertainty in the background estimate.

The expected form of the stellar density distribution in dSphs is unknown, although several profiles have been suggested. It is not our intention to compare the radial distributions in Fig. 3 to every model which has been proposed, and we have instead adopted the simplest, most intuitive and most commonly used. In particular, King profiles are used and the simple, empirical form of these is given by

$$f_{\rm K} = A \left\{ \frac{1}{\left[1 + (r/r_{\rm c})^2\right]^{\frac{1}{2}}} - \frac{1}{\left[1 + (r_{\rm t}/r_{\rm c})^2\right]^{\frac{1}{2}}} \right\}^2 \tag{4}$$

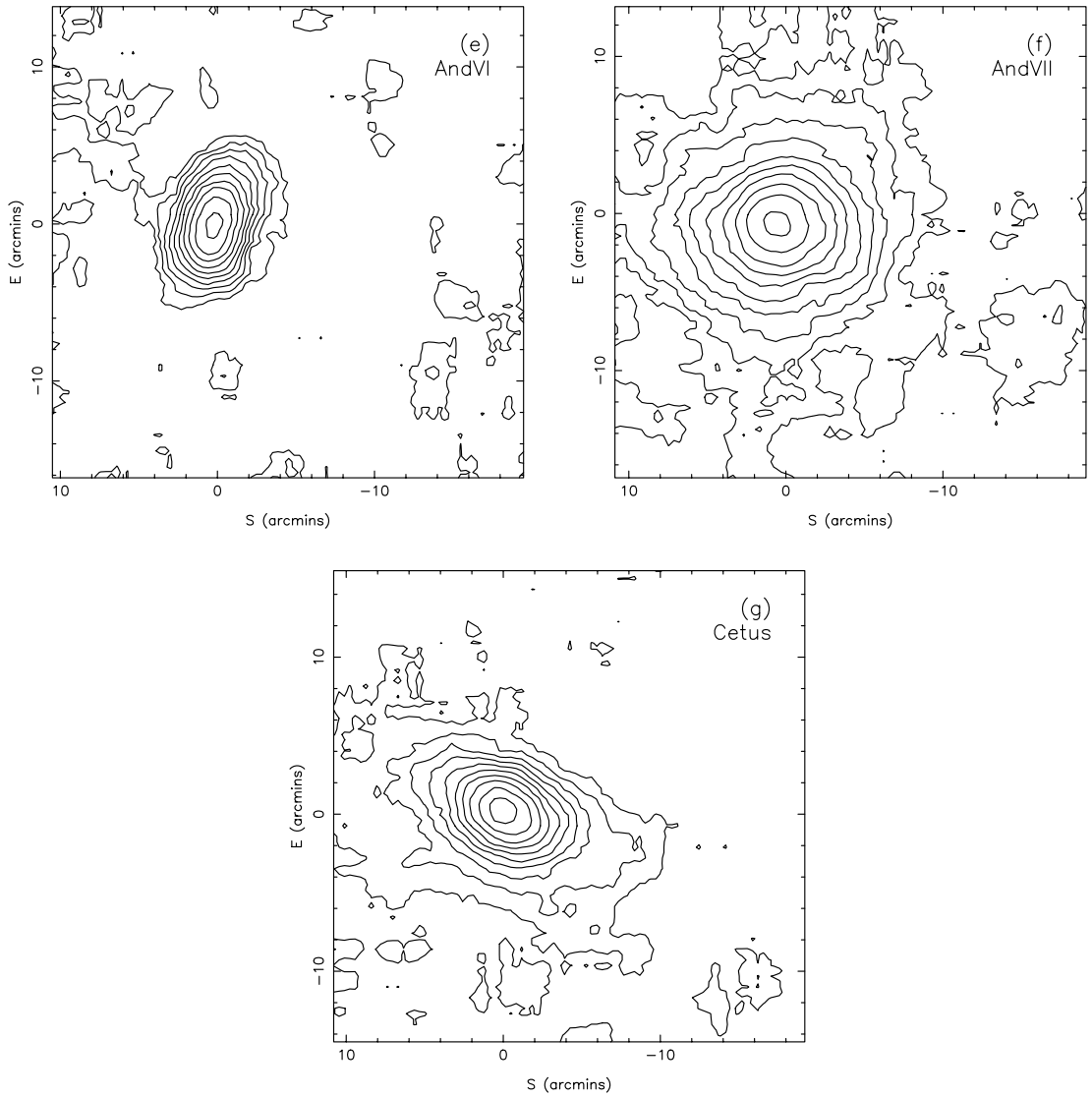

Figure 2 – *continued*

Table 1. Intensity-weighted centres and geometric parameters for the dSphs. Errors are estimated from the variation in the parameters as a function of isophotal threshold. Centres are estimated to be accurate to within ±7 arcsec in both directions.

			Shape parameters	
	RA (x_o)	Dec. (y_o)	PA $= \theta$ (°)	$\epsilon = 1 - b/a$
Andromeda I	$00^{\rm h}45^{\rm m}40.3^{\rm s}$	$+38°02'21''$	22 ± 15	0.22 ± 0.04
Andromeda II	$01^{\rm h}16^{\rm m}28.3^{\rm s}$	$+33°25'42''$	34 ± 6	0.20 ± 0.08
Andromeda III	$00^{\rm h}35^{\rm m}31.1^{\rm s}$	$+36°30'07''$	136 ± 3	0.52 ± 0.02
Andromeda V	$01^{\rm h}10^{\rm m}17.0^{\rm s}$	$+47°37'46''$	32 ± 10	0.18 ± 0.05
Andromeda VI	$23^{\rm h}51^{\rm m}46.9^{\rm s}$	$+24°34'57''$	163 ± 3	0.41 ± 0.03
Andromeda VII	$23^{\rm h}26^{\rm m}33.5^{\rm s}$	$+50°40'48''$	94 ± 8	0.13 ± 0.04
Cetus	$00^{\rm h}26^{\rm m}10.5^{\rm s}$	$-11°02'32''$	63 ± 3	0.33 ± 0.06

(King 1962). A is a scaling parameter, r the radius from the centre of the system, $r_{\rm c}$ is the core radius and $r_{\rm t}$ is the tidal radius. For the range of core concentrations considered here [$c = \log_{10}(r_{\rm t}/r_{\rm c}) < 1.5$], these profiles closely match the physically motivated form derived in King (1966) for globular clusters, which is based on a lowered Gaussian distribution function (Binney & Tremaine 1987). King profiles – both the empirical and physically motivated forms – provide a tractable family of models with intuitive parameters that have been fitted extensively to dwarf galaxies (Hodge 1966; Eskridge 1988a,b; IH95). We therefore adopt them as one of the models to be compared to the radial distributions in Fig. 3, although we note that there is not necessarily a physically motivated reason to expect King profiles to be a realistic form of the radial profile for dwarf galaxies, and interpretations based on this assumption should be treated with caution.

Faber & Lin (1983) advocate exponential profiles to describe the projected surface density distribution of dSphs:

$$f_{\rm E} = B \exp\left(-\frac{r}{r_{\rm e}}\right), \tag{5}$$

where B is a scaling parameter and $r_{\rm e}$ is the effective radius. These models require one parameter less than King models and qualitatively often provide as good a fit as the more complex family. Read & Gilmore (2005) have shown that exponential profiles are a generic phase of dSph evolution if they undergo rapid mass loss at early

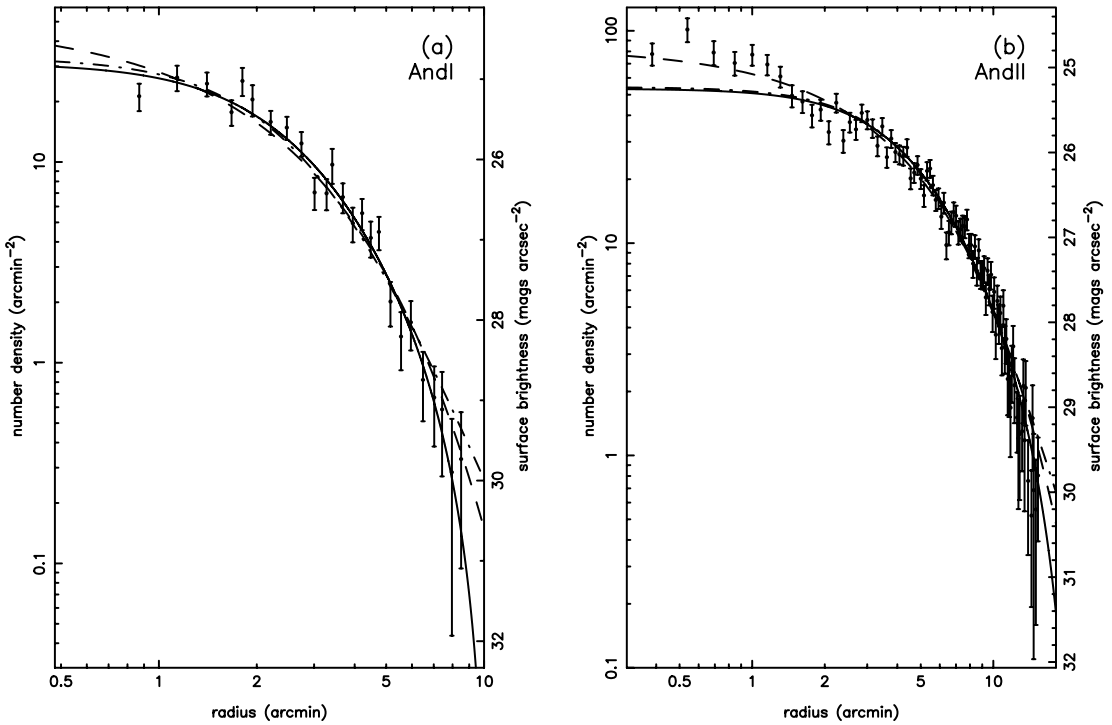

Figure 3. Log–log plots of the stellar radial profiles of the dSph galaxies. Error bars take into account the Poisson uncertainty in the counts and the uncertainty in the background estimate. The solid curves represent the best King profile fit to the data (equation 4, Table 2), the dashed lines correspond to the best exponential fit (equation 5, Table 3) and the dot–dashed lines represent the best Plummer model fit (equation 6, Table 3). The surface brightness scale on the right vertical axis has been calculated by normalizing the data to the integrated flux measurement in Section 3.

times. r_e is a useful parameter, and we additionally compare this class of model to the stellar radial distributions.

Finally, Plummer models are frequently used in *N*-body simulations of dwarf galaxy disruption in a tidal field (e.g. Font et al. 2004; Law, Johnston & Majewski 2005). They are of the form

$$f_P = C\frac{b^2}{(b^2+r^2)^2}, \quad (6)$$

where C is a scaling parameter and b is the Plummer core radius. Due to their common use in simulations, we adopt this as the final model to compare with the dSph profiles.

These three models are fitted to each of the stellar radial profiles using a least-squares minimization technique. The best-fitting King, exponential and Plummer models are overlaid on the logarithmic profiles in Fig. 3 as the solid, dashed and dot–dashed curves, respectively. The derived parameters corresponding to each of these models are listed for each galaxy in Tables 2 and 3, along with the associated uncertainties and the formal value of the reduced χ^2 statistic. The concentration parameter for the King profile is also given. The scaleradii correspond to the geometric mean along the two axes of the dwarf. The surface brightness scale on the right vertical axis of Fig. 3 has been calculated by normalizing the radial profile to the integrated flux measurements described in the following section.

3 INTEGRATED PHOTOMETRY

We have directly estimated the central surface brightness and integrated luminosity of the dSphs from the integrated flux distribution of each galaxy. With suitable image processing, the effects of Galactic foreground stars and random noise can be reduced to manageable levels, enabling these integrated parameters to be measured in a simple manner.

The processing procedure is relatively straightforward. First, the existing object catalogues are used to define a bright foreground star component at least 0.5–1 mags above the TRGB, to allow for the potential presence of AGB stars. A circular aperture is then excised around each foreground star, and the flux within this aperture is set to the local sky level, interpolated from a whole-frame background map. The size of this aperture is the maximum of four times the catalogue-recorded area of the bright star at the detection isophote, or a diameter four times the derived full width at half-maximum (FWHM) seeing. Each frame is then rebinned on a 3×3 grid to effectively create 1-arcsec pixels. The binned image is then further smoothed using a 2D Gaussian filter with a FWHM of 5 arcsec.

The result of this procedure is to produce a coarsely sampled smooth image containing both the resolved and unresolved light contribution from the dSph. The central surface brightness can then be trivially measured by deriving the radial profile, here defined as the median flux value within elliptical annuli. Finally, large elliptical apertures are placed over the dSph and several comparison regions to estimate the background-corrected integrated flux from the dwarf and the reference regions. The variation in the flux from the multiple comparison measures gives a good indication of the flux error, which is, of course, dominated by systematic fluctuations rather than by random noise. To mitigate the effect of random residual foreground stellar haloes and scattered light from bright stars just outside the field of view, the elliptical apertures are chosen to correspond to the derived value of $r_{\frac{1}{2}}$ for the dSph. The estimated total flux is then scaled to allow for this correction. For Andromeda VII, a quarter-light radius is used instead as there is a significant Galactic nebulosity in this field which makes estimates based on larger

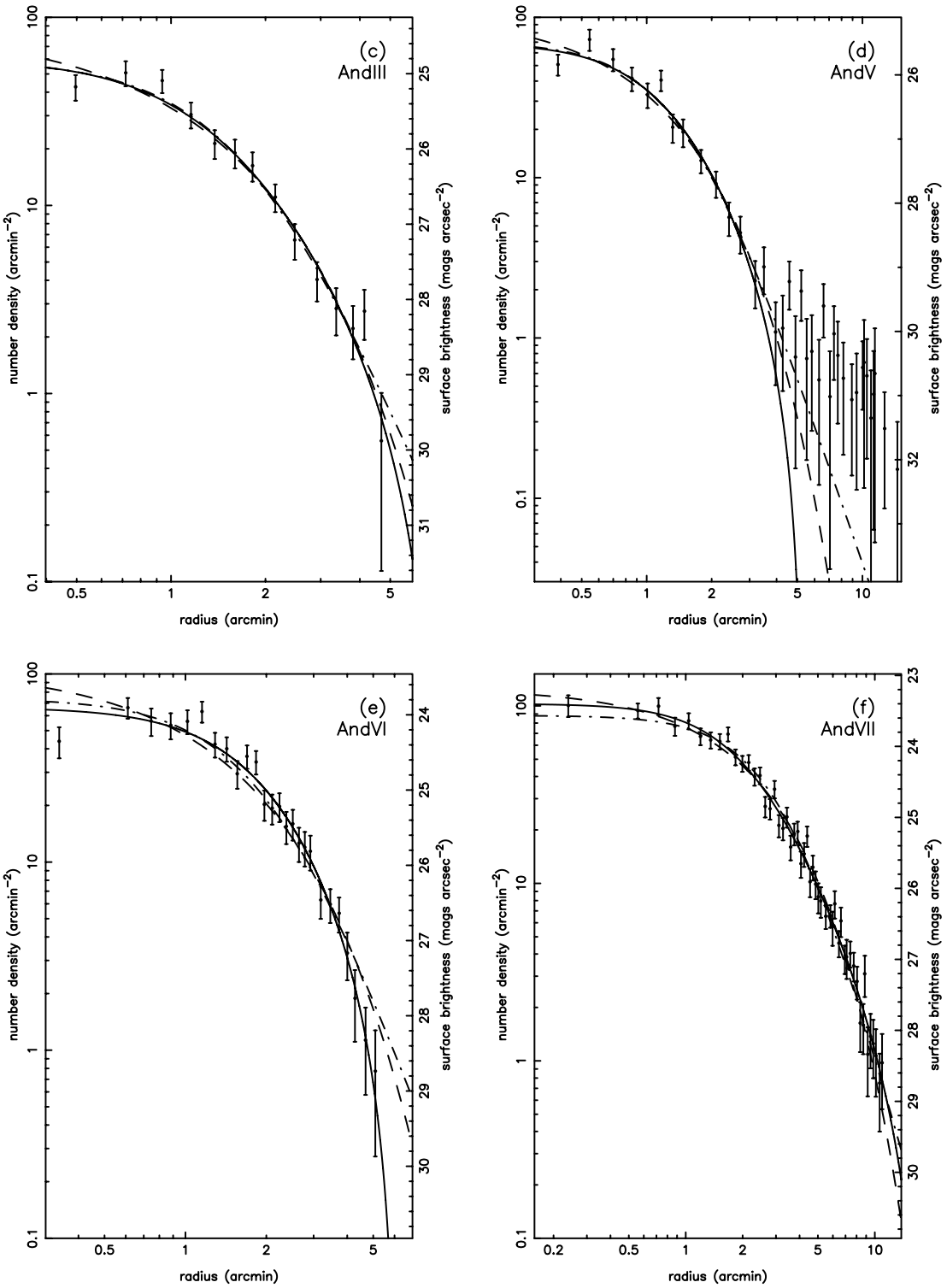

Figure 3 – *continued*

apertures unreliable. As with the resolved component, some of the comparison regions may contain light from the dSph. However, this effect is negligible in comparison to the systematic fluctuation.

The results for each galaxy are listed in Table 4. The integrated apparent magnitude has not been corrected for extinction, but all other quantities are extinction corrected using the values given by Schlegel, Finkbeiner & Davis (1998), tabulated in table 1 of McConnachie et al. (2005). The distance measurements and associated uncertainties derived in McConnachie et al. (2005) have also been used. V_o is the directly measured central surface brightness for the dSphs. S_o is the derived value of the central surface brightness obtained by normalizing the King profile such that the integral under the profile is equal to the integrated magnitude for the dSph. For Andromeda II, a two-component profile has been used instead of the

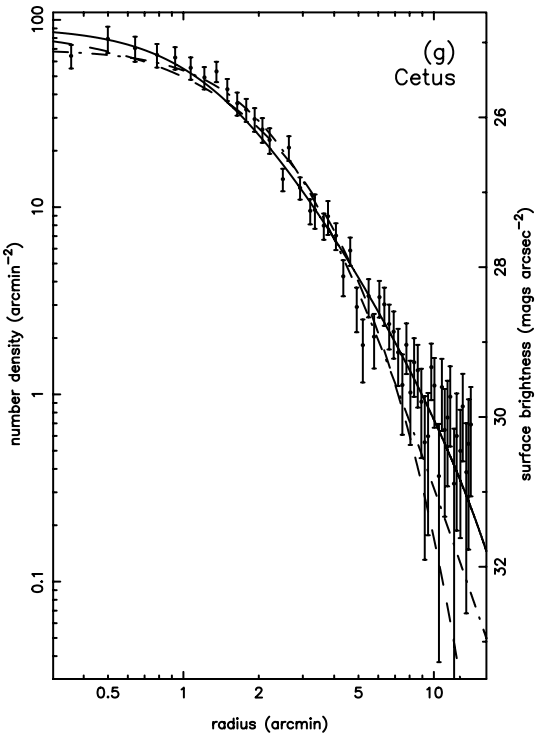

Figure 3 – *continued*

King profile (see Section 4.3). The uncertainty on the measurement of S_o is dominated by the uncertainty on the absolute magnitude for the dSph, and the uncertainty on the directly measured central surface brightness V_o is estimated to be ∼0.1–0.2 mag. There is reasonable agreement between the values for V_o and S_o, which highlights the accuracy and consistency of the integrated magnitude measurement, the radial profiles and the surface brightnesses.

Table 4 also lists the derived values of $r_{\frac{1}{2}}$ of each dSph, obtained by integration of the appropriate King profile. This is with the exception of Andromeda II, where a two-component profile was used, and Cetus, where $r_{\frac{1}{2}}$ has been derived by integration of the exponential profile. The lack of an obvious truncation radius in the Cetus data results in a value for $r_{\frac{1}{2}}$ derived from the King profile which is twice as large as from either the Plummer or exponential profiles and which is probably unreliable. The half-light radius of a Plummer profile is equal to b, and the half-light radius of an exponential profile is $1.68r_e$. Generally, these are consistent with the tabulated value for $r_{\frac{1}{2}}$ measured from the King model fit.

4 DISCUSSION

Figs 2 and 3 and Tables 1, 2, 3 and 4 present many results relating to the Cetus and M31 dSphs. In this section, we compare these results to those of previous studies (Section 4.1), and then discuss each dSph individually (Sections 4.2 and 4.3). We then compare the M31 and Galactic populations (Section 4.4) and examine correlations in the Local Group population as a whole (Section 4.5).

4.1 Comparison with previous work

Caldwell et al. (1992) and Caldwell (1999) derived structural parameters for Andromeda I, II, III, V, VI and VII based upon the integrated light of these galaxies. Whiting, Hau & Irwin (1999) has derived the structural parameters for Cetus. Table 5 lists the values for $r_{\frac{1}{2}}$, m_V and M_V (corrected for the extinction measurements and distances used here) from Caldwell et al. (1992) (Andromeda I, II and III), Caldwell (1999) (Andromeda V, VI and VII) and Whiting et al. (1999) (Cetus). The value of $r_{\frac{1}{2}}$ for Cetus has been evaluated by integrating the King profile in Whiting et al. (1999).

Table 2. Details of the best-fitting King (equation 4) profiles shown in Fig. 3 as the solid curves. Each scaleradius is the geometric mean for the dwarf. The distance moduli and associated uncertainties derived in McConnachie et al. (2005) have been used to transform units.

		King profile				
	χ^2	r_c (arcmin)	r_t (arcmin)	r_c (kpc)	r_t (kpc)	$c = \log_{10}(r_t/r_c)$
Andromeda I	1.01	2.7 ± 0.3	10.4 ± 0.9	0.58 ± 0.06	2.3 ± 0.2	0.59 ± 0.06
Andromeda II	1.84	5.2 ± 0.2	22.0 ± 1.0	0.99 ± 0.04	4.2 ± 0.2	0.63 ± 0.03
Andromeda III	0.89	1.3 ± 0.2	7.2 ± 1.2	0.29 ± 0.04	1.5 ± 0.3	0.74 ± 0.10
Andromeda V	1.02	1.2 ± 0.2	5.3 ± 1.0	0.28 ± 0.04	1.2 ± 0.2	0.63 ± 0.11
Andromeda VI	0.96	2.1 ± 0.2	6.2 ± 0.4	0.48 ± 0.06	1.4 ± 0.1	0.46 ± 0.06
Andromeda VII	0.91	2.0 ± 0.1	19.3 ± 1.6	0.45 ± 0.02	4.3 ± 0.4	0.98 ± 0.04
Cetus	1.00	1.3 ± 0.1	32.0 ± 6.5	0.29 ± 0.02	7.1 ± 1.5	1.40 ± 0.10

Table 3. Details of the best-fitting exponential (equation 5, dashed curves in Fig. 3) and Plummer (equation 6, dot–dashed curves in Fig. 3) models. Each scaleradius is the geometric mean for the dwarf. The distance moduli and associated uncertainties derived in McConnachie et al. (2005) have been used to transform units.

	Exponential profile			Plummer profile		
	χ^2	r_e (arcmin)	r_e (kpc)	χ^2	b (arcmin)	b (kpc)
Andromeda I	1.36	1.72 ± 0.06	0.38 ± 0.02	1.22	3.12 ± 0.12	0.67 ± 0.03
Andromeda II	1.66	3.53 ± 0.06	0.67 ± 0.01	2.14	6.44 ± 0.10	1.23 ± 0.02
Andromeda III	1.00	1.00 ± 0.05	0.24 ± 0.01	0.76	1.82 ± 0.10	0.40 ± 0.03
Andromeda V	1.25	0.86 ± 0.05	0.20 ± 0.01	0.92	1.56 ± 0.08	0.35 ± 0.02
Andromeda VI	2.20	1.20 ± 0.04	0.27 ± 0.01	1.56	2.15 ± 0.08	0.49 ± 0.02
Andromeda VII	1.14	2.00 ± 0.04	0.44 ± 0.01	1.18	3.47 ± 0.07	0.77 ± 0.02
Cetus	2.06	1.59 ± 0.05	0.34 ± 0.02	1.56	2.69 ± 0.08	0.59 ± 0.02

Table 4. The integrated photometric properties of the dSphs. The integrated apparent magnitude (m_V) is uncorrected for reddening, while the absolute magnitudes (m_V) and central surface brightnesses have been dereddened. V_o is the directly measured central surface brightness while S_o is the central surface brightness obtained by normalizing the radial profile to the integrated luminosity of the dSph. The values for $r_{\frac{1}{2}}$ are obtained by integration of the appropriate King profile with the exception of Andromeda II, where a two-component model has been used (see Section 4.3), and Cetus, where the exponential profile has been used.

	Integrated photometry					
	m_V	M_V	V_o	S_o	$r_{\frac{1}{2}}$ (arcmin)	$r_{\frac{1}{2}}$ (kpc)
Andromeda I	12.7 ± 0.1	-11.8 ± 0.1	24.7	24.8	2.8	0.60
Andromeda II	11.7 ± 0.2	-12.6 ± 0.2	24.5	24.7	5.6	1.06
Andromeda III	14.4 ± 0.3	-10.2 ± 0.3	24.8	24.7	1.6	0.36
Andromeda V	15.3 ± 0.2	-9.6 ± 0.3	25.3	25.6	1.3	0.30
Andromeda VI	13.2 ± 0.2	-11.5 ± 0.2	24.1	23.9	1.8	0.42
Andromeda VII	11.8 ± 0.3	-13.3 ± 0.3	23.2	23.6	3.3	0.74
Cetus	13.2 ± 0.2	-11.3 ± 0.3	25.0	24.8	2.7	0.60

Table 5. Previous estimates of $r_{\frac{1}{2}}$, m_V and M_V for the Cetus and M31 dSphs, taken from Caldwell et al. (1992) (Andromeda I, II and III), Caldwell (1999) (Andromeda V, VI and VII) and Whiting et al. (1999) (Cetus). The values for M_V have been recalculated for the distance and reddening estimates used here.

	$r_{\frac{1}{2}}$ (arcmin)	m_V	M_V
Andromeda I	2.5	12.75 ± 0.07	-11.8
Andromeda II	2.3	12.71 ± 0.16	-11.6
Andromeda III	1.3	14.21 ± 0.08	-10.4
Andromeda V	0.6	15.92 ± 0.14	-8.9
Andromeda VI	1.4	13.30 ± 0.12	-11.4
Andromeda VII	1.3	12.90 ± 0.27	-12.2
Cetus	1.4	14.4 ± 0.2	-10.1

We measure $r_{\frac{1}{2}}$ for Cetus to be twice that of Whiting et al. (1999). These authors trace the Cetus surface brightness profile to $\sim$4 arcmin, while the measurement here extends to $\sim$12 arcmin. Additionally, the limiting surface brightness of Whiting et al. (1999) is $\sim$29.5 mag arcsec^{-2} (see their fig. 4), while our profile extends $\sim$1.5 mag arcsec^{-2} deeper. As a result, we find Cetus extends much further than originally measured. The brighter luminosity we derive is fully consistent with this increase in size. Identical arguments apply for Andromeda V and VII, where we measure their radial profiles out to much larger radii and over a larger range in surface brightness than Caldwell (1999), and find them to be more extended and therefore brighter.

A similar reason to the one above is not responsible for the difference in results for Andromeda II. Caldwell et al. (1992) measures the surface brightness profile for this galaxy over a similar radial and surface brightness range as we do, yet we derive a value for $r_{\frac{1}{2}}$ that is more than twice as large as that derived by Caldwell et al. (1992). We believe this is a result of the complexity of the profile of Andromeda II, which we discuss in Section 4.3.

4.2 The isolated dwarf spheroidal in Cetus

In the Local Group, there is a preference for dSph galaxies to be found as satellites of either M31 or the Galaxy, whereas dwarf irregular galaxies are preferentially found in more isolated environments. The origin of this position – morphology relation is not yet known, although it may well be related to the ram pressure and tidal stripping of dwarf galaxies near large galaxies by hot, gaseous haloes

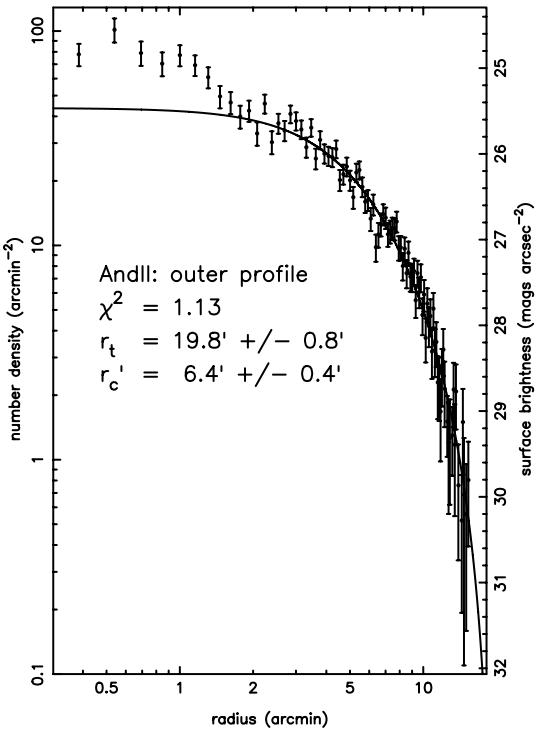

Figure 4. The best-fitting King model to the surface brightness profile of Andromeda II, ignoring the inner 2 arcmin. The formal value of the fit is good, and the divergence of the King profile to the data at small radii suggests the presence of a secondary core component.

(Mayer et al. 2001a,b; 2005). Cetus and Tucana are the only dSph galaxies in the Local Group which are not clearly satellites of either M31 or the Galaxy. Analysis of their properties, and comparison to the dSphs which are satellites, may prove useful in determining the origin of this position – morphology relation and in determining which evolutionary processes can be attributed to environmental effects.

The King model tidal radius of Cetus is $r_t = 6.6$ kpc, making it apparently the largest dSph in the Local Group by a significant amount. However, the stellar radial profile out to 12 arcmin does not show any evidence of turning over, and the derived value of r_t is well beyond the final data point. Therefore, the concept of a tidal radius in this case is probably misleading as Cetus shows no

evidence of tidal truncation. Cetus is currently $\simeq$750 kpc from the Galaxy, which places it $\simeq$680 kpc from M31. If Cetus has spent most of its evolution in isolation then we would not expect it to be truncated; its profile is fully consistent with an undisturbed system. From equation (7) and assuming the masses of M31 and the Galaxy to be $\simeq 10^{12}\,M_{\odot}$, then if Cetus has a typical mass for a dSph ($\sim 5 \times 10^{7}\,M_{\odot}$), the lack of a tidal radius out to 6 or 7 kpc implies that after its last major star formation episode, Cetus has never been much closer that $\sim$200 kpc to either M31 or the Galaxy.

Kinematic information for Cetus is required to compliment this data. A radial velocity measurement may show whether the motion of Cetus suggests it ever having interacted with the Galaxy or M31. In addition, a stellar velocity dispersion measurement will constrain its mass. This information will help decide whether Cetus poses a challenge for formation and gas-loss models of dSphs which currently depend upon interactions with larger systems.

4.3 The M31 dwarf spheroidals

Andromeda I is one of the largest and brightest M31 dSphs and displays the distinctive S-shape indicative of ongoing tidal disruption (Fig. 2a), suggesting the presence of low surface brightness tidal tails. Although the average position angle of Andromeda I is $\sim 22^{\circ}$, its isophotes twist from $\sim 0^{\circ}$ in the centre to $\sim 40^{\circ}$ in the outer regions, again indicating strong tidal disruption (Choi, Guhathakurta & Johnston 2002). From the surface brightness profile alone (Fig. 3a), there is no sign that Andromeda I is being disrupted; there is no indication of a break in the profile, whose presence would normally be interpreted as due to tidal heating/disruption (Choi et al. 2002). Of course, this signature might be found at a lower surface brightness threshold.

Andromeda I shows the strongest evidence of tidal disruption of all the M31 dSphs from its contours alone. Deeper photometry and kinematics of this object will reveal the full extent of its tidal disruption. Kinematic data will be particularly interesting, as it is possible that Andromeda I is surrounded by only a relatively shallow dark matter halo. Otherwise, it is not obvious that the outer stellar regions should be so distorted by the M31 tidal field.

Andromeda II, shown in Fig. 2(b), is huge and circular. It is currently $\simeq$185 kpc from M31 and has a large King tidal radius ($r_{\rm t} = 4.2$ kpc). If its orbit is relatively circular, then this could account for its appearance since the M31 tidal field at this distance should be small. The average ellipticity of Andromeda II is $\simeq$0.22, although its central regions are significantly more circular than this; the innermost three isophotes of Fig. 3(b) are visibly more 'core-like' than its outer regions.

The radial profile of Andromeda II (Fig. 3b) is quite unusual. The formal reduced χ^2 value for the King, Plummer and exponential models is relatively poor; both the King and exponential profiles underestimate the surface brightness in the central few arcmin by nearly a factor of 2, while the Plummer profile also underestimates the central surface brightness slightly while failing to match at intermediate radii. The radius at which the King profile diverges from the data is close to the radius where the 'core' develops in the isopleth map.

Fig. 4 is a King profile fit to the Andromeda II profile ignoring the inner 2 arcmin. The formal quality of the fit is much better in this range ($\chi^2 = 1.13$) and diverges at the same radius at which the 'core' is observed in Fig. 2(b). This reveals a factor of 2 excess of stars at small radius, which is compelling evidence for a second component, in the form of a roughly constant density stellar core. Deeper global photometry down to the level of the horizontal branch and more kinematic information are required to confirm this hypothesis, and place the structure of this galaxy in an evolutionary context. For example, it could be that this represents a dissolved star cluster, or the secondary component may reflect spatial variations in the star formation history, such that there were two main episodes where one led to a more centrally concentrated stellar population than the other. Indeed, from their *HST* study of this galaxy, Da Costa et al. (1996) are unable to model its abundance distribution without assuming a two component ('metal-rich' and 'metal-poor') chemical enrichment model. The above scenarios, however, have only recently started to be considered for the Galactic dSphs, motivated by the discoveries by Kleyna et al. (2004) and Tolstoy et al. (2004).

Andromeda III is the most elongated dSph in this sample. Its outer isophote in Fig. 2(c) suggests that the outer regions of this galaxy may be somewhat stretched and perturbed, although there is no evidence for this in the surface brightness profile (Fig. 3c). Deeper photometry should reveal the true extent of this sparse population. Andromeda III is one the closest dSphs to M31, at a distance of $\simeq$75 kpc.

Andromeda V ($M_V \simeq -9.6$ mag) is a small and faint dSph. The main body of the dwarf is fairly round and compact, but its outermost isophotes appear diffuse and fuzzy (Fig. 2d). It is possible that this is due to heating of the outer region by the tidal field of M31. The radial profile of Andromeda V appears to show a break at 3.5 arcmin, resulting in a failure of all three parametric fits to follow the profile. Simulations show that tidal effects can manifest themselves in the form of a break in the surface brightness profile (Choi et al. 2002), and so Andromeda V may be showing evidence of tidal harassment.

It is also worth noting that the absolute magnitude of Andromeda V which we derive is broadly consistent with a metallicity of [Fe/H] $\simeq -1.5$ (Armandroff et al. 1998; McConnachie et al. 2005). Andromeda V was previously measured to be fainter (Section 4.1), and its original metallicity measurement of [Fe/H] $\simeq -1.5$ by Armandroff et al. (1998) meant that this object was an outlier on the luminosity–metallicity relation first shown by Caldwell (1999). A later measurement marked this object as more metal poor, at [Fe/H] $\simeq -2.2$ (Davidge et al. 2002), more consistent with its low-luminosity measurement. However, the most recent measurement of its metallicity by McConnachie et al. (2005) agrees with the original measurement of Armandroff et al. (1998). Given its absolute magnitude measured here and its higher metallicity measurement, Andromeda V appears to follow the luminosity–metallicity relation of Caldwell (1999), while its earlier discrepancy can be attributed to an underestimated luminosity.

Andromeda VI has a radial profile that is well described by a King profile. It shows no evidence of tidal disruption in either the isopleth map (Fig. 2e) or the surface brightness profile (Fig. 3e). Its $r_{\frac{1}{2}}$ is average for the M31 dSphs, and its M_V and central surface brightness are likewise relatively typical of the population.

Andromeda VII is the brightest and most extended of the M31 dSphs. In a similar way to Andromeda II, Fig. 2(e) shows it to be nearly circular in projection, with an ellipticity of 0.13 and $r_{\rm t} = 4.3$ kpc. Andromeda VII is currently $\sim$220 kpc from M31 and a large tidal radius is not unexpected if its orbit is relatively circular. Unlike Andromeda II, its surface brightness profile shows no deviation from a King model fit.

4.4 Contrasting the M31 and Galactic dwarf spheroidals

The M31 subgroup consists of seven dSph galaxies including Andromeda IX (Zucker et al. 2004; Chapman et al. 2005), compared to nine firmly identified dSphs around the Galaxy. We do not

consider Sagittarius here, however, due to its extreme nature as a highly disrupted system near to the Galactic disc.

IH95, and subsequent authors, found that King and exponential profiles generally fit the surface brightness profiles of the Galactic dSphs very well. For the dSphs analysed here, we find King models are usually marginally better fits than exponential and Plummer profiles, which is not unexpected given that King profiles have an additional parameter. The latter two profiles fit the data equally as well as each other. Six out of eight of the galaxies looked at by IH95 show an excess of stars at large radii in comparison to the best-fitting King model. Of the seven dSphs analysed here, only Andromeda V shows clear evidence of this effect. Interpretation of these stars is a controversial topic in Local Group astronomy. However, in the case of Andromeda V, where the stellar excess is a result of a break in the surface brightness profile, it is likely that this is a manifestation of tidal effects, as shown by Choi et al. (2002). If this can also be shown to be the case for the relevant Galactic dSphs, then this might suggest that the outer regions of the Galactic dSphs are generally more disrupted than the M31 dSphs. However, only small samples are being compared and the evidence is indirect at best; Andromeda I, III and V all hint, to varying degrees, that these galaxies may be tidally perturbed. It should also be noted that the photometry on which the various analyses of the Galactic dSphs are based extends below the main sequence turn-off, whereas the INT WFC photometry of M31 dSphs only samples bright RGB stars.

Fig. 5 shows the absolute magnitude of each dSph plotted against $r_{\frac{1}{2}}$ (left-hand panel) and $r_{\rm t}$ (right-hand panel) for most of the Local Group dSphs. Red squares represent the Galactic dSphs, blue triangles represent the M31 dSphs and Cetus is shown as a magenta diamond. Data are taken from this study, IH95, Zucker et al. (2004) and Harbeck et al. (2005). The half-light radius of Andromeda IX is calculated by integration of the best-fitting King model derived by Harbeck et al. (2005), using the distance calculated in McConnachie et al. (2005). For consistency, we have used the scaleradii corresponding to the single component fit for Andromeda II. Fig. 5 demonstrates that the M31 and Galactic dSphs have a similar range of M_V; the only noticeable difference in this respect is that there are five Galactic satellites with $M_V > -10$ compared to two for M31. Although this is a possible indication of relative incompleteness of the M31 dSph population, the small numbers involved mean that a K–S test shows that the two distributions of M_V are still consistent at the 62 per cent level.

An obvious feature of Fig. 5 is that the values for $r_{\frac{1}{2}}$ and $r_{\rm t}$ of the M31 dSphs are much larger than that for their Galactic counterparts. For a given M_V, the scaleradii of the M31 dSphs are generally twice as large as for the Galactic dSphs. Specifically, the mean and median $r_{\rm t}$ for the M31 dSphs are 2.0 and 2.3 times larger, respectively, than that for the Galactic dSphs and the mean and median $r_{\frac{1}{2}}$ are both 3.1 times larger. The half-light radius, $r_{\frac{1}{2}}$, tracks $r_{\rm c}$, $r_{\rm e}$ and b, and so the same disparity is also seen in these quantities. As these differences are observed across the range of M_V presented by the dSphs, it is unlikely to be an artefact of small number statistics. Instead, these findings point to notable differences between the formation and/or evolution of these dSph populations.

A significant difference in the tidal radius, $r_{\rm t}$, between the two populations will, by default, lead to a difference in the values for $r_{\frac{1}{2}}$. As demonstrated by the value for Cetus, $r_{\rm t}$ depends strongly on environment. The value of $r_{\rm t}$ derived from a King profile fit is not necessarily the true $r_{\rm t}$ for a dSph, but is a useful parametrization to compare with simple analytic models. Oh, Lin & Aarseth (1995) give the following expressions for the value of $r_{\rm t}$ for a dSph in the tidal field induced for a point mass:

$$r_{\rm t} \simeq \frac{(1-e)}{(3+e)^{\frac{1}{3}}} a \left(\frac{M}{M_{\rm h}}\right)^{\frac{1}{3}}, \tag{7}$$

and for a logarithmic halo

$$r_{\rm t} \simeq \left\{\frac{(1-e)^2}{\left[\frac{(1+e)^2}{2e}\right] \ln\left(\frac{1+e}{1-e}\right) + 1}\right\}^{\frac{1}{3}} a \left(\frac{M}{M_{\rm h}}\right)^{\frac{1}{3}}. \tag{8}$$

Here, e is the eccentricity of the orbit of the dSph which has a semimajor axis a. M is the total mass of the dSph and $M_{\rm h}$ is the mass of the host galaxy contained within the current position of the dSph. The details of these equations are not important for the current discussion, and we include them only to highlight the factors on which $r_{\rm t}$ depends. Detailed treatments of $r_{\rm t}$ also require that the orbits of the individual stars in the dSph are taken into account, as stars on radial orbits are preferentially stripped to stars on circular orbits (Read et al. 2005).

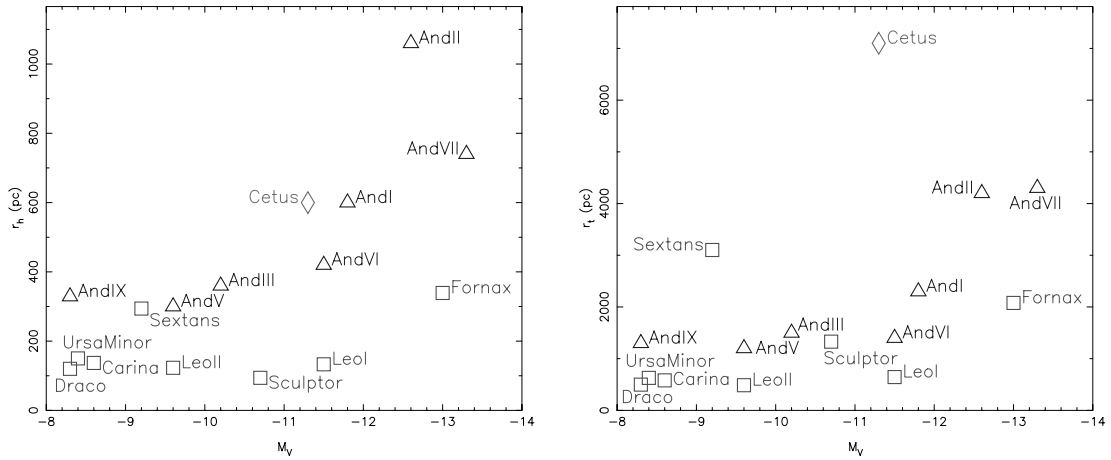

Figure 5. Absolute magnitude versus $r_{\frac{1}{2}}$ (left-hand panel) and $r_{\rm t}$ (right-hand panel) for the Galactic dSphs (red squares), M31 dSphs (blue triangles) and the isolated dSph in Cetus (magenta diamond). For a given M_V, the M31 dSphs have scale radii that are generally at least twice as large as those for the Galactic dSphs.

If we make the plausible assumption that the only fundamental difference between the M31 and Galactic dSphs is that one group orbits M31 and the other group orbits the Galaxy, then the differences in r_t (and the more robust measure $r_{\frac{1}{2}}$) must primarily arise via some combination of the relative distribution of semimajor axes, a, modulated by the orbital eccentricities, e, or the dynamical mass distribution embodied in the parameter M_h. However, it is difficult to break the degeneracy of these factors without more detailed modelling. For example, if M_h as a function of radius is different between M31 and the Galaxy, then so too will the typical values of a. Alternatively, if the characteristic orbits of the two populations have significantly different values for e, then the fraction of the mass of the host galaxy contained within the positions of the dSphs could be very different and change as function of orbital phase, θ. Naively, however, it seems probable that the difference in the typical values of r_t between the dSphs of M31 and the Galaxy is reflecting a difference in $M_h(r, \theta)$ between these two hosts, and requires detailed examination. In this context, it is particularly interesting to note that Huxor et al. (2005) have recently found several extended luminous star clusters in the halo of M31 with large core and tidal radii, which do not have any Galactic counterparts.

4.5 The Local Group population of dwarf spheroidals

The Local Group dwarf galaxies display several correlations between their physical properties. These include correlations between luminosity–halo virial velocity, luminosity–metallicity, spin-parameter–central surface brightness and central surface brightness–luminosity. Dekel & Woo (2003) propose that all of these correlations relate to the role of supernovae feedback in dwarf galaxies, and is an extension of the ideas proposed by Dekel & Silk (1986). The correlation between central surface brightness and luminosity is shown in Fig. 6, and is significant at >99.99 per cent level. While both the M31 and Galactic dSphs show the same trend, the two populations appear offset from one another such that the M31 dSphs have systematically lower central surface brightnesses

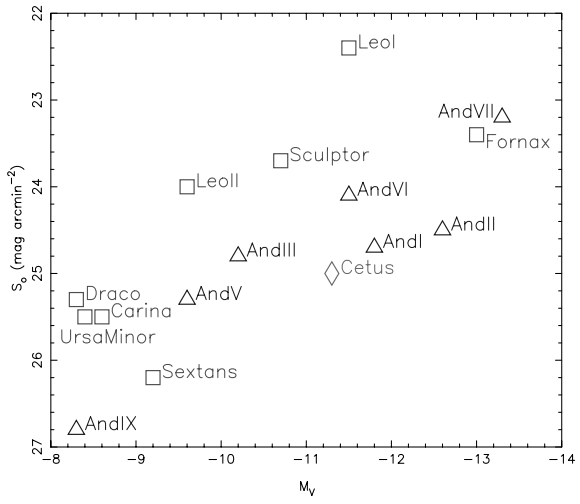

Figure 6. The relation between integrated luminosity and central surface brightness shown by the Local Group dSphs. For the M31 dSphs, the central surface brightness is that which has been directly measured from the integrated flux distribution. For a given M_V, the M31 dSphs have systematically fainter central surface brightnesses, presumably related to their large physical extent.

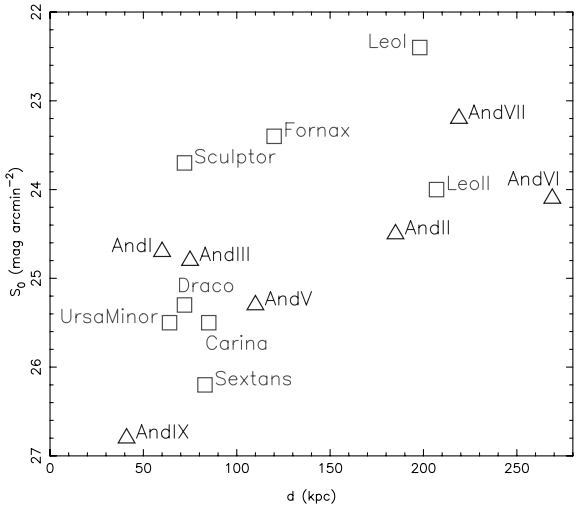

Figure 7. Left-hand panel: central surface brightnesses of the Local Group dSph satellites as a function of distance from the host galaxy. For the M31 dSphs, the central surface brightness is that which has been directly measured from the integrated flux distribution. The central surface brightnesses of the Local Group dSph satellites seem to correlate with their current separation from their host, such that more distant dSphs are brighter. A Spearman rank–order correlation test indicates that this correlation is significant at the 99 per cent level.

for a given M_V. This is presumably related to their more extended nature discussed in the previous section.

Fig. 7 shows the central surface brightness of the Local Group dSph satellites plotted against their distance from the host galaxies. There is an apparent correlation between central surface brightness and current separation, such that brighter dSphs are further from their host. A Spearman rank–order correlation test indicates that this correlation is significant at the 99 per cent level. Due to the correlation between central surface brightness and M_V highlighted previously, there is a secondary correlation between M_V and separation which is significant at the 96 per cent level.

This trend has already been noted for the Galactic satellites; Bellazzini, Fusi Pecci & Ferraro (1996) favoured a physical explanation, whereas Mateo (1998) and van den Bergh (1999) suggested that this reveals that the Galactic satellite system is incomplete at the faint end at large distances. Most recently, Willman et al. (2004) have suggested that some Galactic dSphs fainter than 24 mag arcsec^{-2} at a distance greater than 100 kpc may not have been able to be detected. However, McConnachie & Irwin (2006) argue that Galactic satellites as faint as Sextans would have been found within 200 kpc of the Galaxy in the 2/3 of the sky that were analysed as part of the survey that led to the discovery of Sextans (Irwin et al. 1990). The detection limits of this survey are discussed in detail in Irwin (1994); briefly, for satellites located between ∼30 and ∼400 kpc from the Galaxy, the detectability of their resolved image signature is, to first order, $\propto S_o \times A_o$, where the first term is the central surface brightness and the second term is their scale area. $A_o \propto d^{-2}$ and $S_o \propto d^{1/2}$, implying detectability scales as $d^{-3/2}$. This implies that: Fornax, Sculptor and Leo I would be detectable out to 400 kpc; Leo II would be detectable out to 350 kpc; Carina and Draco out to 300 kpc; Sextans and Ursa Minor out to 250 kpc; satellites one magnitude fainter than Sextans or Ursa Minor would be detected out to 200 kpc. Given this, it is unlikely that the observed trend for the Galactic dSphs is a result of selection effects. Further, the M31 dSphs are here shown to display the same trend as the Galactic dSphs, although different selection

effects apply to this system (McConnachie & Irwin 2006). Clearly, this trend deserves further attention.

It is important to consider the possibility that the correlation between central surface brightness and current separation may be spurious since the observed separation of a dSph from its host galaxy is a function of orbital phase. The current galactocentric distance of a satellite from its host may have no physical relevance in terms of the formation and evolution of that system. To try to quantify this effect, we have examined the Keplerian case of a satellite orbiting a point mass in order to determine for what fraction of an orbital period the instantaneous separation of a satellite from its host is a reasonable estimate of the time-averaged separation. This is equivalent to asking what fraction of a population of satellites on similar orbits will be at a distance from their host which is a reasonable representation of their mean distance, when viewed at a random moment in time.

At a given moment, t, during an orbit of period P, the orbital phase is given by $\theta = t/P$, and we can iteratively solve Kepler's equation for the eccentric anomaly, E,

$$E = 2\pi\theta + e \sin E, \tag{9}$$

for an orbit of eccentricity e. This allows the calculation of the instantaneous radius vector in units of the semimajor axis

$$r' = 1 - e \cos E. \tag{10}$$

The time-averaged separation, $\langle r' \rangle$, of the satellite is then given by

$$\langle r' \rangle = \int_0^1 r' \, \mathrm{d}\theta \tag{11}$$

and the fraction of time, $f_e(\eta)$, for which r' is within a certain fraction of $\langle r' \rangle$ is

$$f_e(\eta) = \int_{\theta_1}^{\theta_2} \eta \, \mathrm{d}\theta. \tag{12}$$

$\eta = r'/\langle r' \rangle$ and (θ_1, θ_2) corresponds to the range of θ for which r' is within the required fraction of $\langle r' \rangle$. The subscript indicates that this is for a specific value of e, and the formalism is readily extended to a range of e since

$$P(\eta) = \frac{\int f_e(\eta) P(e) \, \mathrm{d}e}{\int P(e) \, \mathrm{d}e}. \tag{13}$$

For simplicity, we set $P(e)$ to be constant over some range of e.

Table 6 illustrates the results for four different satellite populations, each with a different spread in e. Oh et al. (1995) estimated the range of e occupied by the Galactic satellites to be $0.3 \leqslant e \leqslant 0.7$. Even for the case where orbits are radially biased, r' is still a reasonable indicator of $\langle r' \rangle$ (i.e. within 33 per cent) in $>2/3$ of the cases. These idealized calculations suggest that a correlation of r' with central surface brightness for the Local Group dSph population implies a similar correlation between $\langle r' \rangle$ and central surface brightness. This then implies that an explanation for the trends is rooted in physics.

Table 6. The fraction of satellites in a population whose current separation from the host is expected to be a reasonable estimate of the time-averaged mean distance, indicated by the fraction $\eta = r'/\langle r' \rangle$, for Keplerian orbits with an even spread in e between the limits indicated. In all cases, the current separation is within 33 per cent of the mean distance most of the time.

		$0.75 \leqslant \eta \leqslant 1.25$	$0.67 \leqslant \eta \leqslant 1.33$
All values	$0 \leqslant e \leqslant 1$	63 per cent	83 per cent
Circularly biased	$0 \leqslant e \leqslant 0.5$	83 per cent	96 per cent
Radially biased	$0.5 \leqslant e \leqslant 1$	44 per cent	70 per cent
Oh et al. (1995)	$0.3 \leqslant e \leqslant 0.7$	52 per cent	80 per cent

Abadi, Navarro & Steinmetz (2005) suggest that, in the current hierarchical paradigm, the dwarf galaxies observed as satellites today were accreted relatively recently, and did not form *in situ*. If this is the case, then the above correlation is unlikely to be a result of the formation of the dwarfs but is more likely to be due to their subsequent evolution. It is difficult to significantly modify the characteristics of the central regions of a dwarf galaxy with an external tidal field, without severely disturbing/disrupting much of the system since the inner regions of dSphs are more tightly bound and shielded than the outer regions (e.g. Oh et al. 1995). The most significant interactions between the satellites and their hosts are gravitational. While ram pressure effects and supernova-driven winds undoubtedly contribute to the development of the baryonic density distribution, it seems likely that gravitational effects play a major role in the evolution of the central surface brightness of satellites as they orbit and interact with their host. These effects are directly amenable to study by numerical simulations.

5 SUMMARY

In this paper, we have derived isopleth maps, surface brightness profiles, intensity-weighted centres, position angles, ellipticities, tidal radii, core radii, concentration parameters, exponential scalelengths, Plummer scalelengths, half-light radii, absolute magnitudes and central surface brightnesses for the Andromeda I, II, III, V, VI, VII and Cetus dSph galaxies. We have shown that the M31 dSph population shows a large variation in morphology, magnitude and radial extent. Andromeda III and V show tentative evidence of tidal harassment, while the morphology of Andromeda I clearly identifies it as a strongly disrupted satellite of M31, suggesting that it may have extended tidal tails and perhaps only a relatively shallow dark matter potential. The isolated dSph in Cetus, on the other hand, does not show any evidence of tidal truncation and has a large radial extent. These results suggest a wide range of tidal effects is experienced by Local Group dSphs. Andromeda II has a clear excess of stars in its central regions and provides compelling evidence for a multiple-component system, similar perhaps to Sculptor or Sextans (Kleyna et al. 2004; Tolstoy et al. 2004). Several of the dSphs are found to be more extended and brighter than previous studies, and in particular Andromeda V is shown to have a luminosity consistent with the metallicity measurements of Armandroff et al. (1998) and McConnachie et al. (2005). Its previous value was consistent with a lower metallicity derived by Davidge et al. (2002).

In general terms, the M31 dSphs show qualitatively similar structural characteristics to the Galactic population. However, the M31 dSphs have much larger scaleradii for a given M_V than the Galactic dSphs, by a factor of 2–3. We suggest that these differences may result from differences in the tidal fields experienced by the two populations, such that the stronger Galactic tidal field truncates its satellites at smaller average radii in comparison to the M31 dSphs which evolve in a comparatively weaker tidal field. This implies the masses of M31 and the Galaxy differ and/or the characteristic orbits of the satellites are different, and requires detailed modelling. In this context, it is particularly interesting to note that Huxor et al. (2005) have recently found several luminous extended star clusters in the halo of M31 with large scaleradii, which do not have any Galactic counterparts. Finally, we highlight a correlation between the central surface brightnesses and the current separations of the dSphs from their hosts, which we argue is due to some unknown physical mechanism, which is most likely dynamical in origin.

ACKNOWLEDGMENTS

This work is based on observations made with the INT on the Island of La Palma by the Isaac Newton Group in the Spanish Observatorio del Roque de los Muchachos of the Institutode Astrofisica de Canarias. We would like to thank the anonymous referee for his/her comments, which led to an improvement in the clarity of this paper. Also, we thank Beth Willman for her feedback on an earlier draft.

REFERENCES

Abadi M. G., Navarro J. F., Steinmetz M., 2005, preprint (astro-ph/0506659)
Armandroff T. E., Davies J. E., Jacoby G. H., 1998, AJ, 116, 2287
Armandroff T. E., Jacoby G. H., Davies J. E., 1999, AJ, 118, 1220
Bellazzini M., Fusi Pecci F., Ferraro F. R., 1996, MNRAS, 278, 947
Binney J., Tremaine S., 1987, Galactic Dynamics. Princeton Univ. Press, Princeton, NJ, p. 747
Caldwell N., 1999, AJ, 118, 1230
Caldwell N., Armandroff T. E., Seitzer P., Da Costa G. S., 1992, AJ, 103, 840
Chapman S. C., Ibata R., Lewis G. F., Ferguson A. M. N., Irwin M., McConnachie A., Tanvir N., 2005, ApJ, 632, L87
Choi P. I., Guhathakurta P., Johnston K. V., 2002, AJ, 124, 310
Da Costa G. S., Armandroff T. E., Caldwell N., Seitzer P., 1996, AJ, 112, 2576
Da Costa G. S., Armandroff T. E., Caldwell N., Seitzer P., 2000, AJ, 119, 705
Da Costa G. S., Armandroff T. E., Caldwell N., 2002, AJ, 124, 332
Davidge T. J., Da Costa G. S., Jørgensen I., Allington-Smith J. R., 2002, AJ, 124, 886
Dekel A., Silk J., 1986, ApJ, 303, 39
Dekel A., Woo J., 2003, MNRAS, 344, 1131
Eskridge P. B., 1988a, AJ, 96, 1352
Eskridge P. B., 1988b, AJ, 95, 1706
Faber S. M., Lin D. N. C., 1983, ApJ, 266, L17
Ferguson A. M. N., Gallagher J. S., Wyse R. F. G., 2000, AJ, 120, 821
Ferguson A. M. N., Irwin M. J., Ibata R. A., Lewis G. F., Tanvir N. R., 2002, AJ, 124, 1452
Font A., Johnston K. V., Guhathakurta P., Majewski S. R., Rich R. M., 2004, preprint (astro-ph/0406146)
Harbeck D. et al., 2001, AJ, 122, 3092
Harbeck D., Gallagher J. S., Grebel E. K., 2004, AJ, 127, 2711
Harbeck D., Gallagher J., Grebel E. K., Koch A., Zucker D., 2005, ApJ, 623, 159
Hodge P. W., 1966, AJ, 71, 204
Huxor A. P., Tanvir N. R., Irwin M. J., Ibata R., Collett J. L., Ferguson A. M. N., Bridges T., Lewis G. F., 2005, MNRAS, 360, 1007
Ibata R., Irwin M., Lewis G., Ferguson A. M. N., Tanvir N., 2001, Nat, 412, 49
Irwin M. J., 1994, in Meylan G., Prugnel P., eds, Proc. ESO Conf. Workshop, Dwarf Galaxies. ESO, Garching, p. 27
Irwin M. J., Trimble V., 1984, AJ, 89, 83
Irwin M., Hatzidimitriou D., 1995, MNRAS, 277, 1354 (IH95)
Irwin M. J., Bunclark P. S., Bridgeland M. T., McMahon R. G., 1990, MNRAS, 244, 16P
Irwin M. J. et al., 2004, in Oschmann J. M., Jr., ed., Proc. SPIE 5493, Ground-Based Telescopes. SPIE, Bellingham, p. 411
Karachentsev I. D., Karachentseva V. E., 1999, A&A, 341, 355
Kerschbaum F., Nowotny W., Olofsson H., Schwarz H. E., 2004, A&A, 427, 613
King I., 1962, AJ, 67, 471
King I. R., 1966, AJ, 71, 64
Kleyna J. T., Wilkinson M. I., Evans N. W., Gilmore G., 2004, MNRAS, 354, 543
Kleyna J. T., Wilkinson M. I., Gilmore G., Evans N. W., 2003, ApJ, 588, L21
Law D. R., Johnston K. V., Majewski S. R., 2005, ApJ, 619, 807
Majewski S. R., Ostheimer J. C., Patterson R. J., Kunkel W. E., Johnston K. V., Geisler D., 2000, AJ, 119, 760
Martínez-Delgado D., Alonso-García J., Aparicio A., Gómez-Flechoso M. A., 2001, ApJ, 549, L63
Mateo M. L., 1998, ARA&A, 36, 435
Mayer L., Governato F., Colpi M., Moore B., Quinn T., Wadsley J., Stadel J., Lake G., 2001a, ApJ, 559, 754
Mayer L., Governato F., Colpi M., Moore B., Quinn T., Wadsley J., Stadel J., Lake G., 2001b, ApJ, 547, L123
Mayer L., Mastropietro C., Wadsley J., Stadel J., Moore B., 2005, preprint (astro-ph/0504277)
McConnachie A., Irwin M., 2006, MNRAS, 365, 902
McConnachie A. W., Irwin M. J., Ferguson A. M. N., Ibata R. A., Lewis G. F., Tanvir N., 2004, MNRAS, 350, 243
McConnachie A. W., Irwin M. J., Ferguson A. M. N., Ibata R. A., Lewis G. F., Tanvir N., 2005, MNRAS, 356, 979
Morrison H. L., Harding P., Hurley-Keller D., Jacoby G., 2003, ApJ, 596, L183
Odenkirchen M. et al., 2001, AJ, 122, 2538
Oh K. S., Lin D. N. C., Aarseth S. J., 1995, ApJ, 442, 142
Palma C., Majewski S. R., Siegel M. H., Patterson R. J., Ostheimer J. C., Link R., 2003, AJ, 125, 1352
Read J. I., Gilmore G., 2005, MNRAS, 356, 107
Read J. I., Wilkinson M. I., Evans N. W., Gilmore G., Kleyna J. T., 2005, preprint (astro-ph/0506687)
Schlegel D. J., Finkbeiner D. P., Davis M., 1998, ApJ, 500, 525
Tolstoy E. et al., 2004, ApJ, 617, L119
van den Bergh S., 1972a, ApJ, 178, L99
van den Bergh S., 1972b, ApJ, 171, L31
van den Bergh S., 1974, ApJ, 191, 271
van den Bergh S., 1999, A&AR, 9, 273
Walton N. A., Lennon D. J., Greimel R., Irwin M. J., Lewis J. R., Rixon G. T., 2001, ING Newsletter, 4, p. 7
Whiting A. B., Hau G. K. T., Irwin M., 1999, AJ, 118, 2767
Willman B., Governato F., Dalcanton J. J., Reed D., Quinn T. 2004, MNRAS, 353, 639
Willman B. et al., 2005, ApJ, 626, L85
Zucker D. B. et al., 2004, ApJ, 612, L121

This paper has been typeset from a TEX/LATEX file prepared by the author.